ISAR Imaging for Nonco-operative Targets Based on Sharpness Criterion Under Low SNR

Zhijun Yang , *Member, IEEE*, Xiaoheng Tan , Weiming Tian , *Member, IEEE*, Xichao Dong , *Member, IEEE*, and Chang Cui , *Member, IEEE*

Abstract—Inverse synthetic aperture radar (ISAR) imaging for noncooperative targets with complex translational motion (TM) and 3-D rotational motion (RM) face the problem of spatial-variant (SV) and high-order phase modulation. The existing ISAR technique cannot compensate for the phase modulation completely, especially under low signal-to-noise ratio (SNR). In this work, an efficient ISAR imaging approach is proposed for non-cooperative targets under low SNR. First, the signal model for noncooperative targets with TM and 3-D RM are established, where the high-order 2-D SV phase error are deduced by utilizing a nonstationary image projection plane model. Second, to mitigate the influence of noise, an adaptive denoising filter is generated by exploring the similarity between the profiles of echoes. In addition, inspired by the characteristic that all scatterers share the same TM, the compensating factors are extracted from the prominent scatterers, which can absolutely avoid the accumulation of residual TM errors. Meanwhile, the signal coherence is fully utilized to compensate for the SV phase errors caused by the RM. Finally, both simulated and electromagnetic data experiments validate the effectiveness and robustness of the proposed method.

Index Terms—Adaptive denoising filter, inverse synthetic aperture radar (ISAR) imaging, low signal-to-noise ratio (SNR), noncooperative targets, nonstationary image projection plane (IPP).

I. INTRODUCTION

INVERSE synthetic aperture radar (ISAR) [1], [2], [3] has the advantages of all-day, all-weather, and remote sensing.

The high-resolution of an ISAR image in range dimension and cross-range dimension, respectively, are obtained by transmitting the signals with large bandwidth and by the relative motion between radar and targets. Besides, the attitude information of targets including size and structure can also be retrieved from the echoes. Therefore, as a vital imaging radar platform, ISAR technology has become increasingly important in many fields such as national defense and geological hazard detection.

For cooperative targets, the attitude remains relatively stable during imaging. In this case, the signal-to-noise ratio (SNR) of echoes is relatively high, and the Doppler frequency is relatively simple. However, for noncooperative targets [4], [5], for example, ship targets under high sea state, the movement usually consists of translational motion (TM) and 3-D rotational motion (RM). Due to TM, its effects would seriously blur ISAR images because all scatterers share the same one. The complex 3-D RM motion including roll, pitch, and yaw obviously decreases the SNR of echoes. In addition, the Doppler frequency of the echoes also presents the characteristic of time-varying, which makes ISAR imaging more challenging.

For noncooperative targets ISAR imaging, many algorithms have been developed, and they can be roughly divided into two categories, e.g., parametric-based and nonparametric-based methods. For the parametric-based approaches, the imaging principle is that the Doppler phases of scatterers in a range cell are modeled as a polynomial phase terms in terms of azimuthal time, e.g., quadratic polynomial or cubic polynomial. As a result, the phase terms of those scatterers are reconstructed by estimating the corresponding coefficients of the polynomial phase with parameter estimation approaches, and several approaches have been developed such as CPF [6], PGCPF [7], CIGCPF [8], IHAF_ICPF [9], to name a few. After reconstructing the signals for all scatterers, high-quality ISAR images are thus obtained. However, those methods are time-consuming because the number of scatterers and the Doppler phase corresponding to each scatterer need to be estimated according to the energy threshold of echoes. The latter is based on joint time-frequency analysis (JFTA) such as short-time Fourier transform (FT) [10] and Wigner-Ville distribution (WVD) [11]. The imaging principle of which is that the echoes in a range cell are processed utilizing the JFTA method, and the well-focused ISAR images are generated joint the time-frequency results in each range cell. However, the JFTA methods would inevitably suffer from serious cross-term interferences. Moreover, the ISAR imaging methods based on the selection of optimal imaging interval [12],

[13], [14] are also widely adopted for noncooperative targets, where the Doppler frequency of echoes are analyzed to select the time interval of relatively stationary as the coherent processing time. Nevertheless, when the sea state is high and the ship body is quickly fluctuating, there may be no desired imaging intervals. Some autofocusing methods including Doppler centroid tracking [15] and phase gradient autofocusing (PGA) [16], are also applied for noncooperative targets imaging. However, they either have a low resolution or need to artificially determine the number of iterations.

Additionally, the existing ISAR imaging methods assume that the TM errors are perfectly compensated for and only consider the RM errors. However, the TM and RM should be compensated simultaneously to meet the requirements of practical applications. The methods of TM compensation (TMC) algorithm are also divided into nonparametric-based and parametric-based methods. The nonparametric-based methods mainly include range alignment and phase adjustment [17], [18], [19], [20]. The parametric-based methods formulate the translational components in the form of high order polynomial [21], [22], [23]. The coefficients of the high-order polynomial are iteratively estimated based on the image indicator, e.g., images entropy and images contrast. However, in this way, the TM errors will be accumulated under low SNR condition, which will affect the compensation of RM error and degrade the ISAR imaging.

To obtain a well-focused ISAR image for noncooperative targets with a complex motion under low SNR, considering the nonstationary characteristic, the signal model of nonstationary image projection plane (IPP) are established. Meanwhile, the TM errors and spatial-variant (SV) phase errors are theoretically derived. By deducing the inherent mechanism between the echoes, the TM errors are compensated. After that, an adaptive denoising filter is developed to mitigate the effect of noise. To compensate the SV phase errors, a novel SC that determines the focusing properties of the scatterers is devised as an indicator for the estimation of motion parameters, and golden section method (GSM) is applied to effectively improve the efficiency of parameter estimation. The main contributions are as follows.

1) To reasonably describe the mobility of the noncooperative targets with TM and 3-D RM, the geometry and signal model with nonstationary IPP are established, where the high-order phase model is deduced to describe the 2-D SV phase errors.
2) By exploring the similarity between the profiles of echoes, an adaptive denoising filter is generated to mitigate the influence of noise for the purpose of extracting prominent scatterers.
3) Compared with the existing TM phase error compensation methods based on parameter estimation, the proposed method fully utilizes the signal itself as a compensating factor, which can absolutely avoid the accumulation of residual errors. Additionally, the signal coherence is fully utilized to compensate for the SV phase errors caused by the RM, and the coherent integration is realized by using the SC.

The rest of this work is organized as follows. In Section II, the geometric and signal model for noncooperative targets with
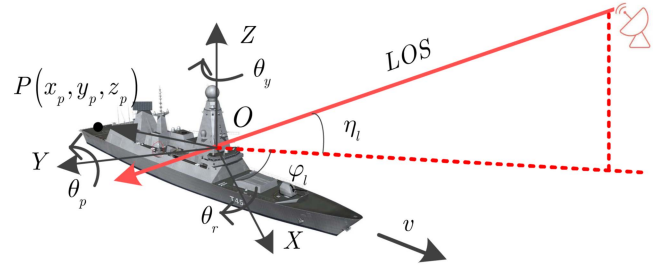

Fig. 1. General geometry model for ship target with complex motion.

nonstationary IPP are introduced, and the imaging problems are also analyzed. An efficient ISAR imaging approach is presented in Section III, where the analysis for the echoes of noncooperative targets, the methods of TMC, the adaptive denoising filter method, and the method for the compensation of SV phase errors, are respectively provided in each section. Some considerations for practical application are presented in Section IV, where the computational complexity, the Doppler frequency, and the phase errors compensation are respectively analyzed. The experimental results and corresponding analysis with simulated and electromagnetic (EM) data are presented in Section V and Section VI concludes this article.

II. IMAGING GEOMETRY AND SIGNAL MODEL FOR NONCOOPERATIVE TARGET

In this section, the ISAR imaging geometry and ship targets with TM and RM are presented for the algorithm developments. The general geometry model of ISAR imaging is depicted in Fig. 1, where the Cartesian coordinate (X, Y, Z) is established in the target body, the origin O is the rotating center, η_l and φ_l denote the elevation and azimuth angles of the radar line-of-sight (LOS), respectively, θ_y, θ_r, and θ_p represent the angular motion yaw, roll, and pitch, and they rotate around Z, X, Y axes, respectively. In addition, the TM velocity of the target is v.

A. Signal Model of Noncooperative Targets With Complex Motion

In this work, the linear frequency modulated (LFM) signals are transmitted, given by

$$s\left(t_r, t_a\right) = \text{rect}\left(\frac{t_r}{T_p}\right) \cdot \exp\left(j2\pi\left(f_c t + \frac{1}{2}K_r t_r^2\right)\right) \quad (1)$$

where $\text{rect}(x) = \begin{cases} 1, |x| \le 1/2 \\ 0, |x| > 1/2 \end{cases}$, t_r, t_a, f_c, K_r, T_p denote the fast time, slow time, carrier frequency, frequency modulation rate, and pulse width, respectively, $t = t_r + m \cdot T_p, (m = 0, 1, \ldots M)$ denotes the full time, and M is the total number of received pulses. In Fig. 1, an arbitrary scatterer P is located on the target body, and its coordinate is denoted by (x_p, y_p, z_p).

With the transmitted LFM signal, the echoes of the scatterer P satisfy

$$s\left(t_r, t_a\right) = \sigma_p \cdot \text{rect}\left(\frac{t_r - 2R_p\left(t_a\right)/c}{T_p}\right)\text{rect}\left(\frac{t_a}{T_a}\right)$$
$$\times \exp\left(j2\pi\left(f_c(t - 2R_p(t_a)/c)\right.\right.$$
$$\left.\left.+ \frac{1}{2}K_r\left(t_r - 2R_p(t_a)/c\right)^2\right)\right) \quad (2)$$

where σ_p, c, T_a denote the reflection coefficient, speed of light, and coherent integration time, respectively. The instantaneous slant range from scatterer P to radar is $R_p(t_a)$ that can be decomposed into TM component $R_t(t_a)$ and RM component $R_r(t_a)$ [25], given by

$$R_p\left(t_a\right) = R_r\left(t_a\right) + R_t\left(t_a\right). \quad (3)$$

The TM component $R_t(t_a)$ can be modeled as a quadratic polynomial in terms of slow time t_a, and it is

$$R_t\left(t_a\right) = R_{p0} + vt_a + \frac{1}{2}\alpha t_a^2 \quad (4)$$

where R_{p0}, v, and α respectively denote the initial range, velocity, and acceleration.

In addition, the RM component $R_r(t_a)$ can be calculated by using the rotational matrix $\mathbf{rot}(t_a)$, given by [26]

$$R_r\left(t_a\right) = \left[\mathbf{rot}\left(t_a\right)\cdot\mathbf{P}\right]^T \cdot \mathbf{i}_{los} \quad (5)$$

where $\mathbf{P} = (x_p, y_p, z_p)$ is the coordinate of the scatterer P, $[\cdot]^T$ denotes the transpose of $[\cdot]$, $\mathbf{i}_{los}$ is the radar LOS, which can be written as

$$\mathbf{i}_{los} = \left[\cos\left(\varphi_l\right)\cos\left(\eta_l\right), \cos\left(\varphi_l\right)\sin\left(\eta_l\right), \sin\left(\varphi_l\right)\right]. \quad (6)$$

For cooperative targets, the attitude of which keeps stable during the coherent processing interval (CPI) [27], which means the IPP is constant. However, for noncooperative targets, they undergo complex 3-D RM and nonstationary IPP during CPI, and existing ISAR imaging algorithms cannot perform well. Therefore, to accurately present the complex motion characteristic for noncooperative targets, the angle of radar LOS is modeled as a linear function with respect to slow time t_a, given by

$$\varphi_l\left(t_a\right) = \varphi_0 + \kappa \cdot t_a$$
$$\eta_l\left(t_a\right) = \eta_0 + \gamma \cdot t_a. \quad (7)$$

Substituting (6) into (7), and using second-order Taylor expansion for trigonometric function yields

$$\mathbf{i}_{los} = \left[i_1\left(t_a\right), i_2\left(t_a\right), i_3\left(t_a\right)\right] \quad (8)$$

where

$$i_1\left(t_a\right) = k_1 + k_2t_a$$
$$i_2\left(t_a\right) = k_3 + k_4t_a \quad (9)$$
$$i_3\left(t_a\right) = k_5 + k_6t_a$$

where

$$k_1 = 1 - \frac{1}{2}\eta_0 - \frac{1}{2}\varphi_0 + \frac{1}{2}\varphi_0\eta_0$$
$$k_2 = -\frac{1}{2}\left(\gamma + \kappa - \frac{1}{2}\varphi_0\gamma - \frac{1}{2}\eta_0\kappa\right)$$
$$k_3 = \eta_0 - \frac{1}{2}\varphi_0\eta_0, k_4 = \gamma - \frac{1}{2}\varphi_0\gamma - \frac{1}{2}\kappa\eta_0 \quad (10)$$
$$k_5 = \varphi_0, k_6 = \kappa.$$

Based on [27], $\mathbf{rot}(t_a)$ can be written as

$$\mathbf{rot}\left(t_a\right) = \begin{bmatrix} a_{11} & a_{12} & a_{13} \\ a_{21} & a_{22} & a_{23} \\ a_{31} & a_{32} & a_{33} \end{bmatrix} \quad (11)$$

where

$$\begin{cases} a_{11} = \cos\left(\theta_p\left(t_a\right)\right)\cos\left(\theta_y\left(t_a\right)\right) \\ a_{12} = -\cos\left(\theta_p\left(t_a\right)\right)\sin\left(\theta_y\left(t_a\right)\right) \\ a_{13} = \sin\left(\theta_p\left(t_a\right)\right) \\ a_{21} = \sin\left(\theta_r\left(t_a\right)\right)\sin\left(\theta_p\left(t_a\right)\right)cos\left(\theta_y\left(t_a\right)\right) \\ \qquad + \cos\left(\theta_r\left(t_a\right)\right)\sin\left(\theta_y\left(t_a\right)\right) \\ a_{22} = -\sin\left(\theta_r\left(t_a\right)\right)\sin\left(\theta_p\left(t_a\right)\right)\sin\left(\theta_y\left(t_a\right)\right) \\ \qquad + \cos\left(\theta_r\left(t_a\right)\right)\cos\left(\theta_y\left(t_a\right)\right) \\ a_{23} = -\sin\left(\theta_r\left(t_a\right)\right)\cos\left(\theta_p\left(t_a\right)\right) \\ a_{31} = -\cos\left(\theta_r\left(t_a\right)\right)\sin\left(\theta_p\left(t_a\right)\right)\cos\left(\theta_y\left(t_a\right)\right) \\ \qquad + \sin\left(\theta_r\left(t_a\right)\right)\sin\left(\theta_y\left(t_a\right)\right) \\ a_{32} = \cos\left(\theta_r\left(t_a\right)\right)\sin\left(\theta_p\left(t_a\right)\right)\sin\left(\theta_y\left(t_a\right)\right) \\ \qquad + \sin\left(\theta_r\left(t_a\right)\right)\cos\left(\theta_y\left(t_a\right)\right) \\ a_{33} = \sin\left(\theta_r\left(t_a\right)\right)\cos\left(\theta_p\left(t_a\right)\right) \end{cases} \quad (12)$$

where

$$\begin{cases} \theta_r\left(t_a\right) \approx \omega_r t_a + \frac{\omega_r'}{2}t_a^2 \\ \theta_p\left(t_a\right) \approx \omega_p t_a + \frac{\omega_p'}{2}t_a^2 \\ \theta_y\left(t_a\right) \approx \omega_y t_a + \frac{\omega_y'}{2}t_a^2 \end{cases}. \quad (13)$$

Substituting (5) into (6)–(13), and using second-order Taylor expansion for trigonometric function, RM component $R_r(t_a)$ can be re-expressed as

$$R_r\left(t_a\right) = K_{p0} + K_{p1}t_a + K_{p2}t_a^2 \quad (14)$$

where

$$K_{p0} = k_1x_p + k_3y_p + k_5z_p$$
$$K_{p1} = \left(x_p\left(k_2 + k_3\omega_y - k_5\omega_p\right) + y_p\left(-k_1\omega_y + k_4 + k_5\omega_r\right)\right.$$
$$\left. + z_p\left(-k_3\omega_r + k_1\omega_p + k_6\right)\right)$$

$$K_{p2} = \begin{pmatrix} x_p\left(-k_1\left(\frac{\omega_p^2}{2} + \frac{\omega_y^2}{2}\right) + \left(\omega_r\omega_y - \frac{\omega_p'}{2}\right)k_5\right. \\ \quad \left. - k_6\omega_p + k_4\omega_y + k_3\left(\frac{\omega_y'}{2} + \omega_p\omega_r\right)\right) \\ + y_p\left(-k_2\omega_y - k_1\frac{\omega_y'}{2} - k_3\left(\frac{\omega_r^2}{2} + \frac{\omega_y^2}{2}\right) + k_6\omega_r\right. \\ \quad \left. + k_5\left(\frac{\omega_r'}{2} + \omega_p\omega_y\right)\right) \\ + z_p\left(-k_4\omega_r - k_3\frac{\omega_r'}{2} - k_5\left(\frac{\omega_p^2}{2} + \frac{\omega_r^2}{2}\right)\right. \\ \quad \left. + \frac{k_1\omega_p'}{2} + k_2\omega_p\right) \end{pmatrix}. \quad (15)$$

From the analysis above, the values of K_{p0}, K_{p1}, K_{p2} are related to the coordinate of the scatterer, which means the RM is accompanied by the characteristic of SV, and the instantaneous slant range $R_p(t_a)$ can be rewritten as

$$R_p\left(t_a\right) = R_r\left(t_a\right) + R_t\left(t_a\right)$$
$$= R_{p0} + vt_a + \frac{1}{2}\alpha t_a^2 + \left[\mathbf{rot}\left(t_a\right)\cdot\mathbf{P}\right]^T \cdot \mathbf{i}_{los}$$

$$\approx R_{p0} + vt_a + \frac{1}{2}\alpha t_a^2 + K_{p0} + K_{p1}t_a + K_{p2}t_a^2. \tag{16}$$

Conducting FT along with t_r in (2), the echoes can be re-expressed as

$$S(f_r, t_a) = \sigma_p \cdot \text{rect}\left[\frac{t_a}{T_a}\right] \cdot$$

$$\times \exp\left(-j2\pi(f_r + f_c)\frac{2\left(R_{p0} + vt_a + \frac{1}{2}\alpha t_a^2\right)}{c}\right)$$

$$\times \exp\left(-j2\pi(f_r + f_c)\frac{2\left(K_{p0} + K_{p1}t_a + K_{p2}t_a^2\right)}{c}\right). \tag{17}$$

B. Problem Presentation

It should be pointed out that, from (17), the phase of the signal in (f_r, t_a) domain is composed of two parts. The former and the latter, respectively, are induced by the TM and RM. Furthermore, both of those phase terms are second-order functions in terms of slow time t_a. To produce high-quality ISAR images, the TM phase and RM phase should be accurately compensated. It is of interest to point out that all scatterers share the same TM components, while the RM errors are determined by the positions of scatterers, which are referred as SV phase errors. For the existing imaging methods, the phase compensation procedure is conducted mainly using the cascading concept. This involves compensating for TM errors first, followed by compensating for RM errors. For TM errors, existing methods either model the TM components as polynomial phase functions with azimuth time or utilize the operation of range alignment and phase adjustment. The image quality indicator of image entropy [28] or image contrast [29] can be used to iteratively align the range profiles and adjust the phase terms. However, using the cascading concept results in estimation errors accumulation [30], especially under low SNRs. Additionally, iterative parameter estimation operations are required during the compensation of both TM and RM error, leading to the increased computational complexity of the algorithms. Therefore, to overcome these limitations, an efficient approach needs to be designed for ISAR imaging of noncooperative targets with complex motions.

III. PROPOSED IMAGING METHOD

A. Signal Analysis

Rewriting (17) gives

$$S(f_r, t_a) = \sigma_p \cdot \text{rect}\left[\frac{t_a}{T_a}\right] \cdot w_a(t_a) \cdot$$

$$\times \exp\left(-j\frac{4\pi(R_{p0} + K_{p0})f_r}{c}\right) \cdot$$

$$\times \exp\left(-j\frac{4\pi(K_{p1} + v)t_a}{\lambda}\right).$$

$$\times \exp\left(-j\frac{4\pi\left((v+K_{p1})t_a + \left(\frac{1}{2}\alpha + K_{p2}\right)t_a^2\right)f_r}{c}\right).$$

$$\times \exp\left(-j\frac{4\pi\left(\frac{1}{2}\alpha + K_{p2}\right)t_a^2}{\lambda}\right).$$

$$\times \exp\left(-j\frac{4\pi(R_{p0} + K_{p0})}{\lambda}\right). \tag{18}$$

It is worthy to be recalled that, from (18), the signal consists of five phase terms. The first phase term and the second one are related to the coordinate in range and azimuth dimensions of scatterers in ISAR image, respectively. The third one is related to the range migration term that should be compensated for. The fourth one is a second-order phase term with slow time. The last one is a constant that can be neglected. Therefore, to produce a high-quality ISAR image, the third and the fourth phase terms should be compensated for. The keystone transform is typically utilized to eliminate the range migration associated with the third phase term. However, the fourth one, which corresponds to the coordinate of the scatterer K_{p2} and acceleration of target α, cannot be completely compensated for at once.

After correcting the range migration term and omitting the constant term, the signal in (18) can be re-expressed as

$$S(f_r, t_a) = \sigma_p \cdot \text{rect}\left[\frac{t_a}{T_a}\right] \cdot w_a(t_a) \cdot$$

$$\times \exp\left(-j\frac{4\pi(R_{p0} + K_{p0})f_r}{c}\right) \cdot$$

$$\times \exp\left(-j\frac{4\pi(K_{p1} + v)t_a}{\lambda}\right) \cdot$$

$$\times \exp\left(-j\frac{4\pi\left(\frac{1}{2}\alpha + K_{p2}\right)t_a^2}{\lambda}\right). \tag{19}$$

Conducting inverse FT (IFT) for $S(f_r, t_a)$ along with f_r yields

$$s(t_r, t_a) = \sigma_p \cdot w_a(t_a) \cdot \text{sinc}\left[B_r\left(t_r - \frac{2(R_{p0}+K_{p0})}{c}\right)\right]$$

$$\cdot \exp\left(-j\frac{4\pi\left(\frac{1}{2}\alpha t_a^2 + vt_a\right)}{\lambda}\right) \cdot \exp\left(-j\frac{4\pi\left(K_{p1}t_a + K_{p2}t_a^2\right)}{\lambda}\right). \tag{20}$$

Performing FT operation in terms of t_a, one obtains

$$s(t_r, f_a) = F_{t_a \to f_a}\{s(t_r, t_a)\}$$

$$= \int_{-\infty}^{\infty} s(t_r, t_a) \cdot \exp(-j2\pi f_a t_a)\, dt_a$$

$$= \sigma_p \cdot \text{sinc}\left[B_r\left(t_r - \frac{2(R_{p0} + K_{p0})}{c}\right)\right] \cdot$$

$$\times \text{sinc}\left[T_a\left(f_a - \frac{K_{p1}}{\lambda}\right)\right]$$

$$\otimes_{t_a \to f_a}\{\Gamma(\alpha, v)\} \otimes_{t_a \to f_a}\{\Gamma(K_{p2})\} \tag{21}$$

where $F_{t_a \to f_a}\{\cdot\}$ denotes the FT operator along with t_a, $\otimes_{t_a \to f_a}\{\cdot\}$ is the convolution operator along with t_a, $\Gamma(\alpha, v)$

and $\Gamma(K_{p2})$, respectively, can be written as

$$\Gamma(\alpha, v) = F_{t_a \to f_a} \left\{ \exp\left(-j4\pi\left(\frac{1}{2}\alpha t_a^2 + vt_a\right)\bigg/\lambda\right)\right\} \tag{22}$$

$$\Gamma(K_{p2}) = F_{t_a \to f_a} \left\{ \exp\left(-j4\pi\left(K_{p2}t_a^2\right)/\lambda\right)\right\}. \tag{23}$$

It should be pointed out that, the term $\otimes_{t_a \to f_a}\{\Gamma(\alpha, v)\}$ and $\otimes_{t_a \to f_a}\{\Gamma(K_{p2})\}$ could seriously blur the ISAR images. Therefore, to obtain well-focused ISAR images, the phase term $\exp(-j4\pi(\frac{1}{2}\alpha t_a^2 + vt_a)/\lambda)$ and $\exp(-j4\pi(K_{p2}t_a^2)/\lambda)$ must be compensated. The former is caused by the TM, which is shared by all scatterers and can be compensated for at once. The latter one, on the other hand, is caused by the 3-D RM and introduces completely different phase errors for each scatterer. Therefore, it is necessary to compensate for these errors accurately by taking into account the coordinate of each pixel [31].

B. Adaptive Denoising Processing

Due to the complex motion of the scatterers, such as the presence of TM and 3-D RM, the SNR of echoes are obviously decreased. Consequently, to extract prominent scatterers for the purpose of TM error compensation introduced in the next section, the effect of noise should be suppressed.

Motivated by the characteristic that the profiles of the echoes have similarities in CPI, in this work, an efficient adaptive denoising window filter is designed to suppress the strong noise, and it can be defined as

$$h(t_r) = \frac{\sum_{a=1}^{M} |s(t_r, t_a)|}{\max\left\{\sum_{a=1}^{M} |s(t_r, t_a)|\right\}} \tag{24}$$

where $h(t_r)$ denotes the adaptive denoising window filter, $\max\{\cdot\}$ is the maximum. Of particular note is that, in (24), the filter works on the amplitude and does not change the phase of the signals.

After filtering out the noise by using the filter $h(t_r)$, the signals $\tilde{s}(t_r, t_a)$ can be expressed as

$$\tilde{s}(t_r, t_a) = s(t_r, t_a) \cdot h(t_r) \tag{25}$$

where $\tilde{s}(t_r, t_a)$ is

$$\tilde{s}(t_r, t_a) = \sigma_p' \cdot w_a(t_a) \cdot \text{sinc}\left[B_r\left(t_r - \frac{2(R_{p0} + K_{p0})}{c}\right)\right] \cdot$$
$$\times \exp\left(-j\frac{4\pi\left(\frac{1}{2}\alpha t_a^2 + vt_a\right)}{\lambda}\right) \cdot$$
$$\times \exp\left(-j\frac{4\pi\left(K_{p1}t_a + K_{p2}t_a^2\right)}{\lambda}\right) \tag{26}$$

where σ_p' represents the amplitude of the signals after filter processing.

C. TM Compensation

Based on the analysis above, in this work, the signal in a specified range cell that contains prominent scatterers are

selected as the compensation factors of TM phase error. Thanks to the internal mechanism in the echoes, the initial range R_{p0}, velocity v and, acceleration α do not need to be estimated. The advantage of this operation is that the TM errors can be completely compensated for and the real-time performance of ISAR imaging can be guaranteed. In addition, the accumulated errors caused by the operation of multiply parameters estimation for the compensating of TM and RM phase errors are avoided.

In general, amplitude normalized variance (ANV) is utilized to evaluate the existence of a prominent scatterer in a specified range bin. The ANV of mth range bin can be defined as [32]

$$\delta_m = 1 - \frac{|E\{|\tilde{s}(t_r^m, t_a)|\}|^2}{E\{|\tilde{s}(t_r^m, t_a)|^2\}} \tag{27}$$

where $E\{\cdot\}$ denotes the expectation operator, $\tilde{s}(t_r^m, t_a)$ represents the signal in mth range bin. The small the δ_m that compared with those in the other range bins, the more likely the prominent scatterer contained in the mth range bin.

Suppose the signal $\tilde{s}(t_r^{m_1}, t_a)$ in m_1th range bin that contains a prominent scatterer is selected, and it can be written as

$$\tilde{s}(t_r^{m_1}, t_a) = \sigma_p^{m_1} \cdot w_a(t_a) \cdot \text{sinc}\left[B_r\left(t_r - \frac{2(R_{p0} + K_{p0})}{c}\right)\right] \cdot$$
$$\times \exp\left(-j\frac{4\pi\left(vt_a + \frac{1}{2}\alpha t_a^2\right)}{\lambda}\right) \cdot$$
$$\times \exp\left(-j\frac{4\pi\left(K_{p1}^{m_1} \cdot t_a + K_{p2}^{m_1} \cdot t_a^2\right)}{\lambda}\right) \tag{28}$$

where $\sigma_p^{m_1}$ denotes the amplitude in m_1th range bin, $K_{p1}^{m_1}$ and $K_{p2}^{m_1}$ respectively are the first-order and second-order coefficients of the phase term caused by the RM.

Furthermore, the signals $\tilde{s}(t_r^{m_2}, t_a)$ in m_2th range bin can be expressed as

$$\tilde{s}(t_r^{m_2}, t_a) = \sigma_p^{m_2} \cdot w_a(t_a) \cdot \text{sinc}\left[B_r\left(t_r - \frac{2(R_{p0} + K_{p0})}{c}\right)\right] \cdot$$
$$\times \exp\left(-j\frac{4\pi\left(vt_a + \frac{1}{2}\alpha t_a^2\right)}{\lambda}\right) \cdot$$
$$\times \exp\left(-j\frac{4\pi\left(K_{p1}^{m_2} \cdot t_a + K_{p2}^{m_2} \cdot t_a^2\right)}{\lambda}\right) \tag{29}$$

where $\sigma_p^{m_2}$ denotes the amplitude in m_2th range bin, $K_{p1}^{m_2}$ and $K_{p2}^{m_2}$ are respectively the first-order and second-order coefficients of the phase term induced by the RM.

By multiplying the conjugate of $\tilde{s}(t_r^{m_2}, t_a)$ and $\tilde{s}(t_r^{m_1}, t_a)$, and the resulting signal is

$$\bar{s}(t_r^{m_2}, t_a) = \tilde{s}(t_r^{m_2}, t_a) \cdot \tilde{s}^*(t_r^{m_1}, t_a)$$
$$= \tilde{\sigma}_p \cdot w_a(t_a) \cdot \exp\left(-j\frac{4\pi\left(\left(K_{p1}^{m_2} - K_{p1}^{m_1}\right)t_a\right)}{\lambda}\right) \cdot$$
$$\times \exp\left(-j\frac{4\pi\left(\left(K_{p2}^{m_2} - K_{p2}^{m_1}\right)t_a^2\right)}{\lambda}\right) \tag{30}$$

where $\tilde{s}^*(t_r^{m_1}, t_a)$ represents the conjugate of $\tilde{s}(t_r^{m_1}, t_a)$, $\bar{s}(t_r^{m_2}, t_a)$ denotes the product of $\tilde{s}^*(t_r^{m_1}, t_a)$ and $\tilde{s}(t_r^{m_2}, t_a)$, respectively, $\tilde{\sigma}_p$ stands for the amplitude after the conjugate multiplication.

What is noteworthy is that, from (30), the phase errors induced by the TM are completely compensated for in $\bar{s}(t_r^{m_2}, t_a)$. Obviously, there are two phase terms present in $\bar{s}(t_r^{m_2}, t_a)$. The first phase term represent the Doppler center of the scatterers. Actually, compared with the Doppler center in (29), the initial location $K_{p1}^{m_2}$ has shifted to $K_{p1}^{m_1}$, which does not affect the focusing of the Doppler phase in the azimuth dimension. The second one is the SV phase error because it is completely different from each other in the pixel domain. To compensate those phase errors, the parameters $(K_{p2}^{m_2} - K_{p2}^{m_1})$ must be accurately estimated.

D. SV Phase Errors Compensation

After conducting the compensation of the TM phase errors, the SV phase error terms $\exp[-j4\pi((K_{p2}^{m_2} - K_{p2}^{m_1})t_a^2)/\lambda]$ in (30) should be precisely compensated for. Due to the SV characteristic for each scatterers, the parameters $(K_{p2}^{m_2} - K_{p2}^{m_1})$ in different range bins are also different. Accordingly, to estimate the parameters $(K_{p2}^{m_2} - K_{p2}^{m_1})$ in all range bins, the compensation terms can be constructed as

$$H_r(\mu, t_a) = \exp\left(j4\pi\mu t_a^2/\lambda\right) \tag{31}$$

where μ is an arbitrary constant.

Performing the compensation with $H_r(\mu, t_a)$ in (30) yields

$$\hat{s}(t_r^{m_2}, t_a) = \bar{s}(t_r^{m_2}, t_a) \cdot H_r(\mu, t_a)$$

$$= \tilde{\sigma}_p \cdot w_a(t_a) \cdot \exp\left(-j\frac{4\pi\left((K_{p1}^{m_2} - K_{p1}^{m_1})t_a\right)}{\lambda}\right) \cdot$$

$$\times \exp\left(-j\frac{4\pi\left(((K_{p2}^{m_2} - K_{p2}^{m_1}) - \mu)t_a^2\right)}{\lambda}\right) \tag{32}$$

where $\hat{s}(t_r^{m_2}, t_a)$ denotes the signal after the compensation of SV phase errors. The second phase term denotes the residual phase error term after conducting SV phase error compensation.

With an iterative search for the parameter μ, the SV phase error terms can be accurately estimated in m_2th range bins. The sharpness S of the ISAR images that determines the focusing performance of scatterers is defined as the criterion for estimating the optimal parameter μ_{optimal}, and it is [33]

$$S = \arg\max_{\mu}$$

$$\times \left\{ \sum_{f_a} \left| F_{t_a \to f_a}\left\{\bar{s}(t_r^{m_2}, t_a) \cdot \exp\left(j4\pi\left(\mu t_a^2\right)/\lambda\right)\right\} \right|^4 \right\} \tag{33}$$

where $\sum_{f_a} |\cdot|$ denotes the summation along with f_a, $\max_{\mu}\{\cdot\}$ represents the maximum value in terms of the parameter μ. During the compensation process of SV phase errors, the change of the parameter $\delta_i = |\mu_i - (K_{p2}^{m_2} - K_{p2}^{m_1})|$ is reflected by the
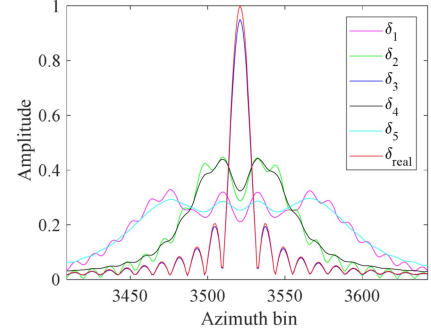

Fig. 2. Schematic diagram of parameter search.

change of sharpness S, where the larger S is, the smaller the residual phase error $\exp(-j4\pi(((K_{p2}^{m_2} - K_{p2}^{m_1}) - \mu_i)t_a^2)/\lambda)$ is, the closer μ is to the true value, shown in Fig. 2, where $\delta_i(i = 1, 2, \ldots, 5)$ can be utilized to denote the estimated parameter and δ_{real} denotes the real parameter. As a result, when the estimated parameter, e.g., δ_3, is closer to the real parameter $(K_{p2}^{m_2} - K_{p2}^{m_1})$, e.g., δ_{real}, the sharpness S reach a maximum.

By using the iterative search for the parameter μ_{optimal}, the SV phase error terms in m_2th range bin are perfectly compensated for, and it is

$$\tilde{s}(t_r^{m_2}, t_a) = s(t_r^{m_2}, t_a) \cdot H_r^i(\mu_{\text{optimal}}, t_a)$$

$$= \tilde{\sigma}_p \cdot \exp\left(-j\frac{4\pi\left((K_{p2}^{m_2} - K_{p2}^{m_1})t_a\right)}{\lambda}\right). \tag{34}$$

Conducting FT operation in terms of t_a for (34), it can be written as

$$s(f_a) = F_{t_a \to f_a}\{\tilde{s}(t_a)\}$$

$$= \tilde{\sigma}_p \cdot \text{sinc}\left[f_a - (K_{p1}^{m_2} - K_{p1}^{m_1})\right]. \tag{35}$$

By combining (21) with (35), the scatterers in m_2th range bin are focused in the location of $(R_{p0} + K_{p0}, K_{p1}^{m_2} - K_{p1}^{m_1})$ in the ISAR images.

Furthermore, as explained above, the SV phase errors are determined by the space coordinates and motion parameters of scatterer. Therefore, the optimal parameter μ_{optimal} should be estimated one by one for each range bin. Meanwhile, the optimal parameter μ_{optimal} in a specified range bin should be iteratively estimated. However, in a real-world application, echoes consist of multiple range bins, and this operation can be time-consuming. In terms of this issue, the GSM is adopted to improve imaging efficiency.

As a result, the realization procedure of the proposed method is as follows.

Step 1) The raw echoes $s(t_r, t_a)$ of the targets are received by radar.

Step 2) Finishing the range compression obtains $s(f_r, t_a)$.

Step 3) Correcting the range migration via using keystone transform gives $s(t_r, t_a)$.

Step 4) Appling the adaptive de-noising filter $h(t_r)$ to suppress the noise and the resulting signal is denoted by $\tilde{s}(t_r, t_a)$.
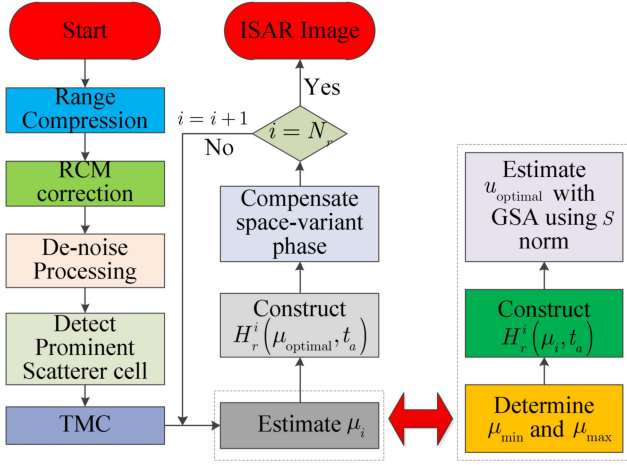
Fig. 3.   ISAR imaging procedure of the proposed method.

Step 5) Extracting the signal $\tilde{s}(t_r^{m_1}, t_a)$ with prominent scatterers via the ANV method.

Step 6) Using $\tilde{s}(t_r^{m_1}, t_a)$ to compensate for the TM phase error produces $\bar{s}(t_r^{m_2}, t_a)$.

Step 7) Constructing compensation factors of SV phase errors term $H_r(\mu, t_a)$ and using the sharpness S as an image quality indicator for ISAR imaging to accurately estimate the optimal parameter μ_{optimal} in m_2th range bin. In addition, using the GSM can improve the imaging efficiency.

Step 8) Iteratively estimate the optimal parameter μ_{optimal} in all range bins, and obtain the high-quality ISAR images.

Finally, the realization procedure of the proposed approach for non-cooperative target ISAR imaging is summarized in Fig. 3.

IV. SOME CONSIDERATIONS IN APPLICATION

A. Computational Complexity Analysis

In this section, the computational complexities of PGA, WVD, IHAF_ICPF, and the proposed method are theoretically analyzed. In general, some procedures with low-computational complexity are neglected, and $N\log_2(N)$ floating-point operations (FLOPs) are needed to compute N-point FT or IFT, and N FLOPs are needed to calculate one-time complex multiplication for N-point data. Suppose the size of the ISAR image is $(N_r \times N_a)$.

The imaging procedure of the PGA method consists of coarsely range-Doppler (RD) imaging, center shifting operation, windowing operation, phase gradient estimation, and iterative phase errors correction. The computational complexity of coarsely RD imaging composed of range compression and azimuth compression is, $O[2N_aN_r \log_2(N_r) + N_aN_r + N_rN_a \log_2(N_a)]$. The computational cost of center shifting operation, windowing operation, phase gradient estimation, and iterative phase error correction are $O[N_aN_r]$, $O[N_rN_a \log_2(N_a)]$, $O[2N_aN_r]$, and $O[N_rN_a \log_2(N_a)]$, respectively. In addition, the computational load of range migration correction is $O[N_aN_r]$. Therefore, the

total computational complexity of the PGA method is

$$C_{PGA} = O \begin{bmatrix} 3N_rN_a\log_2(N_a) + 5N_aN_r \\ + 2N_aN_r\log_2(N_r) \end{bmatrix}. \quad (36)$$

The realization procedure of the WVD method consists of range compression, range cell migration correction, and TF processing in azimuth dimension. The computational complexity of range compression and range migration correction respectively are $O[2N_aN_r \log_2(N_r) + N_aN_r]$ and $O[N_aN_r]$. WVD method is a nonlinear transformation method, and the computational load for N_a-point data is $O\{4N_a^3 + N_a^2 \log_2(N_a)\}$. Therefore, the total computational cost of the WVD method is

$$C_{WVD} = O \left\{ \begin{array}{l} 2N_aN_r\log_2(N_r) + 2N_aN_r \\ + N_r \left(4N_a^3 + N_a^2 \log_2(N_a)\right) \end{array} \right\}. \quad (37)$$

The IHAF_ICPF method in [9] is utilized to estimate the amplitude and phase of scatterers in a specified range bins. Meanwhile, the phase term is modeled as a cubic polynomial function. The computational complexities for the estimation of third-order coefficient, second-order coefficient, and first-order coefficient are $O\{N_a^4\}, O\{N_a^3\}, O\{N_a \log_2(N_a)\}$, respectively. Besides, the computational complexity of range compression and range migration correction are $O[2N_aN_r \log_2(N_r) + N_aN_r]$ and $O[N_aN_r]$, respectively. Suppose there are P scatterers in arbitrary range bin, and the total computational complexity of the IHAF_ICPF method is

$$C_{IHAF\_ICPF} = O \left\{ \begin{array}{l} 2N_aN_r\log_2(N_r) + 2N_aN_r \\ + N_rP \left(N_a^4 + N_a^3 + 2N_a \log_2(N_a)\right) \end{array} \right\}. \quad (38)$$

According to the imaging procedure provided in Fig. 3, the computational complexities of range compression and range migration correction of the proposed method are $O[2N_aN_r \log_2(N_r) + N_aN_r]$ and $O[N_aN_r]$, respectively. The computational load of adaptive denoising operation, extracting range cell with single prominent scatterer and TM correction respectively are $O\{2N_rN_a\}$, $O\{N_rN_a\}$ and $O\{N_rN_a\}$. Suppose the number of optimal parameter estimation with GSM is L, and thus the computational cost is $O\{N_r(L(N_a + N_a \log_2(N_a)) + N_a + N_a \log_2(N_a))\}$. Therefore, the computational complexity of the proposed method is

$$C_{PROP} = O \left\{ \begin{array}{l} 2N_aN_r\log_2(N_r) + 6N_aN_r \\ + N_r \left((L+1)(N_a + N_a \log_2(N_a))\right) \end{array} \right\}. \quad (39)$$

It can be observed, from Table I, that the PGA method takes the least computational time, followed by the proposed method. The third one is the WVD method, and IHAF_ICPF takes the most time. Obviously, compared with WVD and IHAF_ICPF, the proposed method has an advantage in terms of imaging efficiency. In addition, compared with the proposed method, although the computational complexity of the PGA method is superior, its imaging performance is not comparable.

B. Doppler Frequency Analysis

The Doppler frequency for noncooperative targets with complex motions is analyzed in this section. Based on (1), the

Methods	Computational Complexity
PGA	$C_{PGA} = O\begin{vmatrix} 3N_r N_a \log_2 N_a + 5N_a N_r \\ + 2N_a N_r \log_2 N_r \end{vmatrix}$
WVD	$C_{WVD} = O\begin{Bmatrix} 2N_a N_r \log_2 N_r + 2N_a N_r \\ + N_r \ 4N_a^3 + N_a^2 \log_2 N_a \end{Bmatrix}$
IHAF_ICPF	$C_{IHAF\_ICPF} = O\begin{Bmatrix} 2N_a N_r \log_2 N_r + 2N_a N_r \\ + N_r P \ N_a^4 + N_a^3 + 2N_a \log_2 N_a \end{Bmatrix}$
Proposed Approach	$C_{PROP} = O\begin{Bmatrix} 2N_a N_r \log_2 N_r + 6N_a N_r \\ + N_r \ L+1 \ N_a + N_a \log_2 N_a \end{Bmatrix}$

Doppler frequency can be expressed as

$$
\begin{aligned}
f_d(t_a) &= -\frac{1}{2\pi} \frac{d\{\phi(t_a)\}}{dt_a} \\
&= \frac{2}{\lambda} \frac{d\{R_p(t_a)\}}{dt_a} \\
&= f_d^{trans}(t_a) + f_d^{rotat}(t_a) \\
&= \frac{2}{\lambda}\{v + \alpha t_a\} + \frac{2}{\lambda}\{M_x \cdot x_p + M_y \cdot y_p + M_z \cdot z_p\}
\end{aligned}
\tag{40}
$$

where $f_d^{trans}(t_a)$ and $f_d^{rotat}(t_a)$ respectively, denote the Doppler frequency caused by the TM and RM of noncooperative targets, and $\phi(t_a) = -4\pi R_p(t_a)/\lambda$, M_x, M_y and M_z, respectively, can be written as (41), (42), and (43) shown at the bottom of this page.

Based on (40), the Doppler frequency of the noncooperative targets with complex motion consists of $f_d^{trans}(t_a)$ and $f_d^{rotat}(t_a)$, where the Doppler frequency $f_d^{trans}(t_a)$ induced by

the TM is the same for all scatterers. Meanwhile, the Doppler frequency $f_d^{rotat}(t_a)$ caused by the RM is related to the positions of scatterers, which presents SV features. Therefore, the Doppler frequency $f_d(t_a)$ of noncooperative targets is accompanied by the time-varying characteristic.

C. Phase Errors Compensation Analysis

During TMC, the existence of noise may lead to extra phase errors, given by

$$
\begin{aligned}
s(t_r^{n1}, t_a) &= \sigma_p^{n1} \cdot \exp\left(-j\frac{4\pi\left(vt_a + \frac{1}{2}\alpha t_a^2\right) + \varepsilon_{n1}^1}{\lambda}\right) \cdot \\
&\times \exp\left(-j\frac{4\pi\left(K_{p1}^{n1} t_a + K_{p2}^{n1} t_a^2\right) + \varepsilon_{n1}^2}{\lambda}\right)
\end{aligned}
\tag{44}
$$

where ε_{n1}^1 and ε_{n1}^2 denote the phase errors caused by the TM and RM, respectively.

Substituting (30) into (44), the signal can be expressed as

$$
\begin{aligned}
s(t_r^{n2}, t_a) &= s(t_r^{n2}, t_a) \cdot s^*(t_r^{n1}, t_a) \\
&= \sigma_p^{n2} \cdot \sigma_p^{n1} \cdot \exp\left(-j\frac{4\pi\left(K_{p1}^{n2} - K_{p1}^{n1}\right)t_a}{\lambda}\right) \cdot \\
&\times \exp\left(j\frac{4\pi\left(K_{p2}^{n1} - K_{p2}^{n2}\right)t_a^2}{\lambda}\right) \cdot \exp\left(j\phi(\triangle\varepsilon)\right)
\end{aligned}
\tag{45}
$$

where $\phi(\triangle\varepsilon)$ represents the angle errors after TMC.

Based on the analysis of the adaptive denoising filter, the amplitude of the noise is suppressed. By doing so, the signal

$$
M_x = \begin{pmatrix}
-\left(\frac{\eta\varphi}{2} - \eta + t_a\left(\frac{\eta\kappa+\gamma\varphi}{2} - \gamma\right)\right)\left(\omega_y + 2\left(\frac{\omega_y'}{2} + \omega_p\omega_r\right)t_a\right) \\
+\left(\frac{\omega_p^2+\omega_y^2}{2}t_a^2 - 1\right)\left(\frac{\gamma+\kappa}{2} - \frac{\eta\kappa+\gamma\varphi}{4}\right) - \kappa\left(\left(\frac{\omega_p'}{2} - \omega_r\omega_y\right)t_a^2 + \omega_p t_a\right) \\
-\left(\frac{\eta\kappa+\gamma\varphi}{2} - \gamma\right)\left(\left(\frac{\omega_y'}{2} + \omega_r\omega_p\right)t_a^2 + \omega_y t_a\right) - \left(\varphi + \kappa t_a\right)\left(\omega_p + 2t_a\left(\frac{\omega_p'}{2} - \omega_r\omega_y\right)\right) \\
+2t_a\left(\frac{\eta+\varphi}{2} - \frac{\eta\varphi}{4} - 1 + \left(\frac{\gamma+\kappa}{2} - \frac{\eta\kappa+\gamma\varphi}{4}\right)t_a\right)\left(\frac{\omega_p^2+\omega_y^2}{2}\right)
\end{pmatrix}
\tag{41}
$$

$$
M_y = \begin{pmatrix}
+2\left(\frac{\omega_r^2+\omega_y^2}{2}\right)t_a\left(\frac{\eta\varphi}{2} - \eta + t_a\left(\frac{\eta\kappa+\gamma\varphi}{2} - \gamma\right)\right) \\
+\kappa\left(\left(\frac{\omega_r'}{2} + \omega_p\omega_y\right)t_a^2 + \omega_r t_a\right) + \left(\varphi + \kappa t_a\right)\left(\omega_r + 2t_a\left(\frac{\omega_r'}{2} + \omega_p\omega_y\right)\right) \\
+\left(\frac{\eta\kappa+\gamma\varphi}{2} - \gamma\right)\left(\frac{\omega_r^2+\omega_y^2}{2}t_a^2 - 1\right) + \left(\frac{\omega_y't_a^2}{2} + \omega_y t_a\right)\left(\frac{\gamma+\kappa}{2} - \frac{\eta\kappa+\gamma\varphi}{4}\right) \\
+\left(\frac{\eta+\varphi}{2} - \frac{\eta\varphi}{4} - 1 + \left(\frac{\gamma+\kappa}{2} - \frac{\eta\kappa+\gamma\varphi}{4}\right)t_a\right)\left(\omega_y + \omega_y't_a\right)
\end{pmatrix}
\tag{42}
$$

$$
M_z = \begin{pmatrix}
\left(\omega_r + \omega_r't_a\right)\left(\frac{\eta\varphi}{2} - \eta + t_a\left(\frac{\eta\kappa+\gamma\varphi}{2} - \gamma\right)\right) \\
-\left(\frac{\omega_p't_a^2}{2} + \omega_p t_a\right)\left(\frac{\gamma+\kappa}{2} - \frac{\eta\kappa+\gamma\varphi}{4}\right) - \kappa\left(\frac{\omega_p^2+\omega_r^2}{2}t_a^2 - 1\right) \\
+\left(\frac{\eta\kappa+\gamma\varphi}{2} - \gamma\right)\left(\frac{\omega_r't_a^2}{2} + \omega_r t_a\right) - \left(\varphi + \kappa t_a\right)2t_a\left(\frac{\omega_p^2}{2} + \frac{\omega_r^2}{2}\right) \\
-\left(\frac{\eta+\varphi}{2} - \frac{\eta\varphi}{4} - 1 + \left(\frac{\gamma+\kappa}{2} - \frac{\eta\kappa+\gamma\varphi}{4}\right)t_a\right)\left(\omega_p + \omega_p't_a\right)
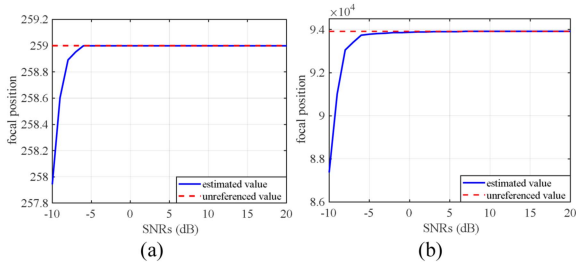\end{pmatrix}.
\tag{43}
$$

Fig. 4. Schematic diagram of coordinate and amplitude with different SNRs. (a) Coordinate. (b) Amplitude.

Fig. 5. Effect of filter on the focusing of scatterers. (a) Slice in azimuth dimension. (b) Slice in range dimension.

can be rewritten as

$$
\tilde{s}\left(t_r^{n2}, t_a\right) = \sigma_p' \cdot \exp\left[-j\frac{4\pi\left(K_{p1}^{n2} - K_{p1}^{n1}\right)t_a}{\lambda}\right] \cdot
$$
$$
\times \exp\left(j\frac{4\pi\left(K_{p2}^{n1} - K_{p2}^{n2}\right)t_a^2}{\lambda}\right) \cdot \exp\left(j\phi\left(\triangle\varepsilon\right)\right)
\tag{46}
$$

where σ_p' is the amplitude of signal after filter processing. It should be noted that σ_p' is less than the maximum amplitude in (45).

Now, suppose the SV phase error terms have been compensated for, and the signal can be written as

$$
\tilde{s}\left(t_r^{n2}, t_a\right) = \sigma_p' \cdot \exp\left[-j\frac{4\pi\left(K_{p1}^{n2} - K_{p1}^{n1}\right)t_a}{\lambda}\right]
$$
$$
\cdot \exp\left(j\vartheta\left(\Delta\varepsilon\right)\right)
\tag{47}
$$

where $\vartheta(\Delta\varepsilon)$ denotes the residual phase error that contains the TM and RM compensation errors.

Conducting FT for (47) with t_a produces

$$
s\left(t_r^{n2}, f_a\right) = F_{t_a \to f_a}^{-1}\left\{\tilde{s}\left(t_r^{n2}, t_a\right)\right\}
$$
$$
= \sigma_p' \cdot \delta\left(f_a - \left(\left(K_{p1}^{n2} - K_{p1}^{n1}\right) + \vartheta\left(\triangle\varepsilon\right)\right)\right) \cdot
\tag{48}
$$

Fig. 4(a) and (b), respectively, provide the focal positions and corresponding amplitude for the scatterer with SNRs from -10 to 20 dB, where the experiments are conduct with 500 runs, the solid blue line and red dotted line, respectively, represents the estimated value and unreferenced value. It is indicated that, from Fig. 4, the noise has a small effect on the scatterer's position in the image. However, the noise can affect the focused amplitudes of scatterers under low SNRs, from -10 to -6 dB. Furthermore, consider the magnitude of the amplitude is 10^4, the influence of noise on the focused amplitude is also relatively small. Therefore, based on the analysis above, the proposed method has a powerful anti-noise performance.

D. Analysis of Filter Windows for Weak Scatterers

It is worthy to be noted that, from (26), the filter affects the amplitude σ_p'. Therefore, to analyze the effect of the filter on weak scatterer, in this section, the system parameters of radar and
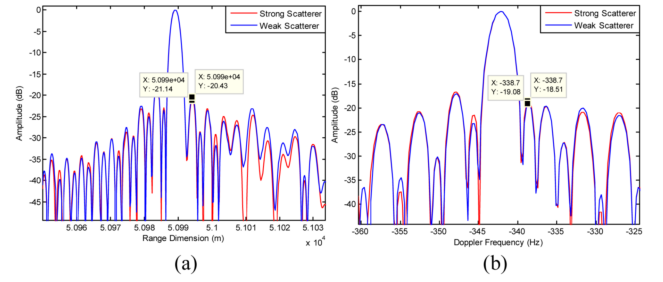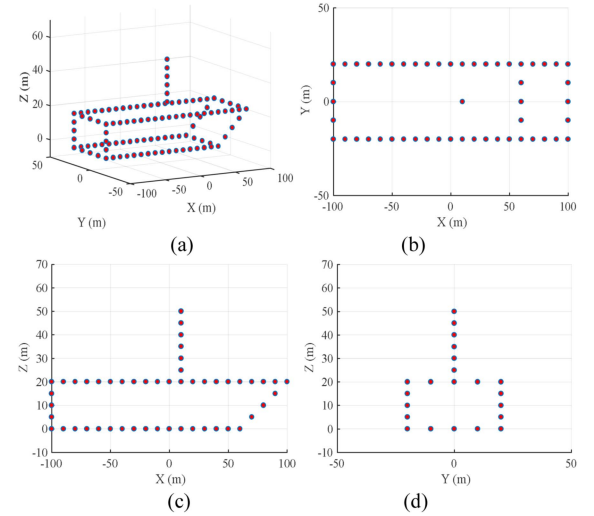

Fig. 6. Three-dimensional model of ship targets. (a) Three-dimensional model. (b) Top view. (c) Left view. (d) Rear view.

motion parameters of targets are provided in Section V-A. Furthermore, the SNR of echoes is 5 dB. In contrast, the amplitudes of echoes for strong scatterers and weak scatterers, respectively, are set as 1 and 0.5. The imaging performance of the same scatterer is analyzed, shown in Fig. 5, where the range slice and azimuth slice are provided in Fig. 5(a) and (b), respectively. It is indicated that the sidelobe of the strong scatterer is 0.71 dB smaller than that of the weak scatterer in range dimension, shown in Fig. 5(a), and the sidelobe of the strong scatterer is 0.57 dB smaller than that of the weak scatterer in Doppler dimension, shown in Fig. 5(b). Therefore, the real value filter has a small influence on the imaging results of weak scatterer that can be ignored.

V. EXPERIMENTAL RESULTS

In this section, the simulated and EM data are utilized to verify the effectiveness of the proposed method. Meanwhile, to present the effectiveness of the proposed method, the results obtained with the proposed method are compared with those of the classical ISAR imaging approaches, e.g., autofocus method (PGA), time-frequency analysis method (WVD), and parameter estimation approach (IHAF_ICPF).
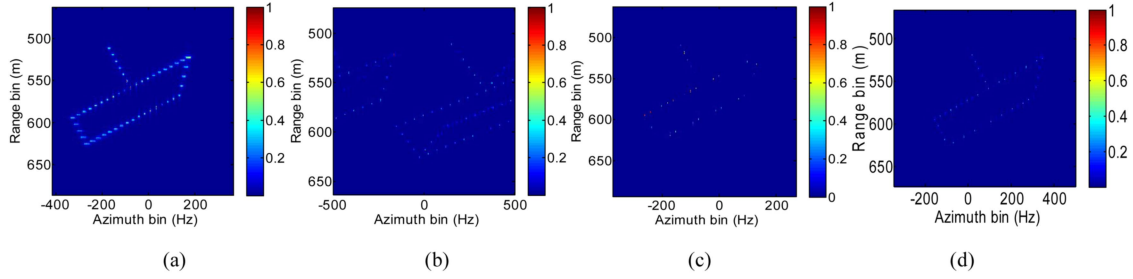
Fig. 7. Imaging results with different methods. (a) PGA method. (b) WVD method. (c) IHAF_ICPF method. (d) Proposed method.
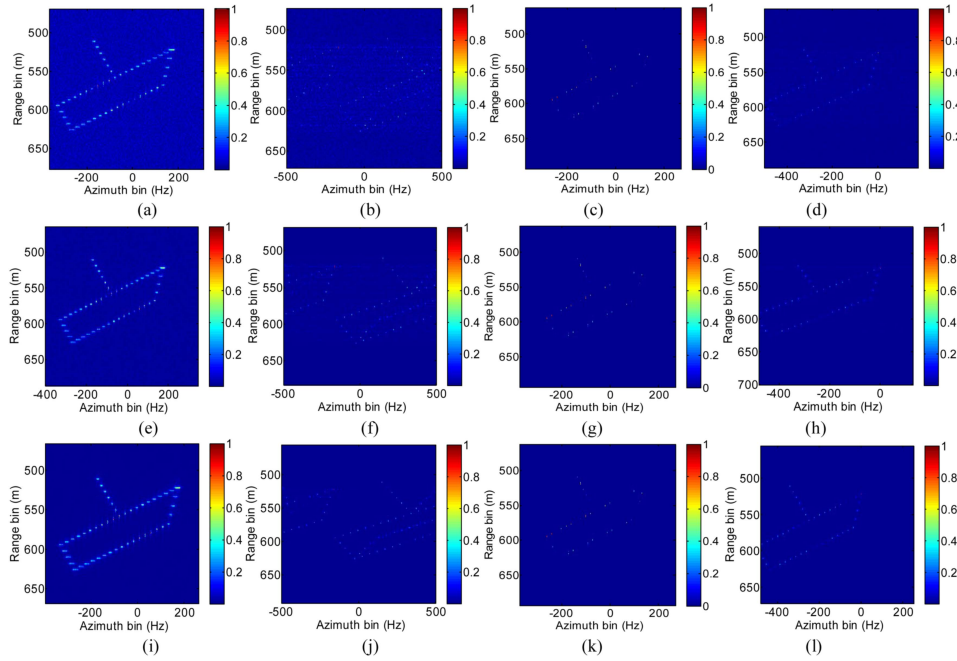

Fig. 8. Imaging results with different methods under different complex white Gaussian noises. (a)–(d) The imaging results of PGA, WVD, IHAF_ICPF and the proposed method under SNR $= -14$ dB, respectively. (e)–(h) Imaging results of PGA, WVD, IHAF_ICPF and the proposed method under SNR $= -7$ dB, respectively. (i)–(l) Imaging results of PGA, WVD, IHAF_ICPF and the proposed method under SNR $= 0$ dB, respectively.

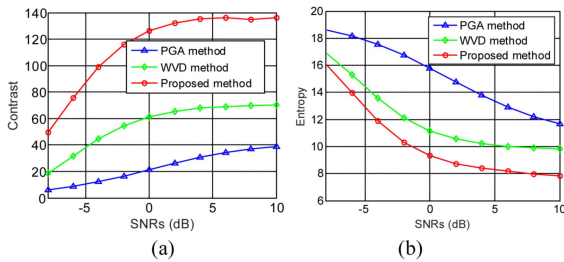Fig. 9. Image entropy and contrast against different SNRs. (a) Image entropy. (b) Image contrast.

TABLE II
SYSTEM PARAMETERS

Parameters	Value	Parameters	Value
Carrier frequency	5 GHz	Pulse width	1 μs
PRF	1000 Hz	Range samples	1500
Bandwidth	500 MHz	Azimuth samples	640

A. ISAR Imaging With Simulated Experiments

The simulated echoes are generated for non-cooperative moving ship targets using the radar system parameters and the motion parameters of targets provided in Tables II and III, respectively.

The 3-D model of the ship targets is shown in Fig. 6, where Fig. 6(a)–(d), respectively, are the 3-D model, top view, left view, and rear view of the ship target. The imaging results obtained using PGA, WVD, IHAF_ICPF, and the proposed method are provided in Fig. 7(a)–(d), respectively. As is shown in Fig. 7, the PGA method produces defocused images, and the WVD method results in serious cross-term interference and broadened reconstructed ISAR images. Although both the IHAF_ICPF

TABLE III
TARGET MOTION PARAMETERS

Target RM parameters (rad/s)					
ω_y	ω_p	ω_r	ω_r'	ω_y'	ω_p'
-0.121	0.1	-0.01	3.5e-2	5.5e-2	-0.025
Target TM parameters					
Velocity (m/s)			Acceleration (m/s²)		
10			1		

TABLE IV
COMPARISON OF IMAGE ENTROPY, CONTRAST, AND IMAGING TIME

Method \ Items	PGA	WVD	IHAF _ICPF	Proposed Method
Entropy	10.47	8.99	--	7.5787
Contrast	42.73	86.14	--	178.804
Time/s	0.67	32.08	185576.95	2.2

method and the proposed method can reconstruct the contour of the ship target, the proposed method offers clearer focusing performance, as shown in Fig. 7(d).

To further demonstrate the validity of the proposed method, the image entropy IE and image contrast IC are used to indicate the focal performance, and they are defined by

$$IE = -\sum_{m=1}^{M}\sum_{n=1}^{N} \frac{|g(m,n)|^2}{G} \log \frac{|g(m,n)|^2}{G} \qquad (49)$$

where $G = \sum_{m=1}^{M}\sum_{n=1}^{N}|g(m,n)|^2$, $g(m,n)$ denotes the m and nth pixel of the ISAR image.

$$IC = \frac{\sqrt{E\left\{(g^2(m,n) - E(g^2(m,n)))^2\right\}}}{E\{g^2(m,n)\}} \qquad (50)$$

where $E\{\cdot\}$ denotes the expectation operator.

The image entropy, contrast, and imaging time for PGA, WVD, IHAF_ICPF, and the proposed method are provided in Table IV, where MATLAB 2014a on an Intel(R) Core(TM) i5-8400 CPU @ 2.8 GHz, and 8 GB RAM, and Microsoft Window 10 operating system is used. The signals of scatterers are reconstructed using the IHAF_ICPF method by estimating the number, amplitude, and phase for all scatterers with the threshold of energy, and there are zero values in the imaging results if the reflected energies of the scatterers are small. Consequently, the image entropy and contrast for the imaging results of the IHAF_ICPF method cannot be calculated. What is noteworthy is that, from Table IV, the image entropy for the imaging results of the proposed method is less than that of the PGA, WVD. In addition, the contrast for the imaging results of our proposed method is larger than that of the PGA and WVD method, which means that the clarity of the imaging results with the proposed method is higher than the PGA and WVD methods. Moreover,

the imaging times of those methods are consistent with the theoretical analysis presented in Section IV-A. Therefore, taking the tradeoff between the imaging performance and the computational complexity into consideration, the proposed method is promising.

B. Performance Analysis in the Presence of Noise

In this section, the white Gaussian noise is added to the echoes (after range compression) to verify the anti-noise performance, and the SNR is defined as

$$\text{SNR} = 10 \log_{10}\left(\frac{\text{Mean power of signal}}{\text{Power of noise}}\right). \qquad (51)$$

Fig. 8 provides the imaging results under different SNRs of -14, -7, and 0 dB. The imaging results of PGA, WVD, IHAF_ICPF, and the proposed method are shown in Fig. 8. It should be pointed that, from Fig. 8, compared with the other three approaches, the proposed method presents a better anti-noise performance, especially the noise suppression for the background of the targets, shown in Fig. 8(d), (h), and (l).

To further evaluate the anti-noise performance, 100 Monte Carlo simulations are conducted against different SNRs to obtain the average of image entropy and contrast. The image entropy and contrast for the imaging results of PGA, WVD, and the proposed method are, respectively, depicted in Fig. 9(a) and (b). It can be seen from Fig. 9 that the image entropy of the proposed method is less than that of the PGA and WVD method, and the contrast of our proposed method is higher than that of the PGA and WVD. Therefore, it can be concluded that the proposed method has an advantage in noisy environments compared with the PGA and WVD.

C. ISAR Imaging With Different Motion Parameters

To further verify the effectiveness, the ISAR imaging results under the conditions of different motion parameters are presented in Fig. 10, where the model is as Fig. 6, and the motion parameters of targets are provided in Table V. It is clearly indicated that the defocusing of the imaging results with PGA method is obviously under different motion parameters, shown in Fig. 10(a), (e), and (i). Furthermore, the imaging results of WVD are broadening in azimuth dimension and the structure of the ship body is shifted in azimuth dimension, provided in Fig. 10(b), (f), and (j). In addition, the contour of the ship target can also be reconstructed, shown in Fig. 10(c), (g), and (k). However, the focused performance is poorer than that of the proposed method. Besides, the imaging results with the proposed method are provided in Fig. 10(d), (g), and (l), where the target body is clearly reconstructed under different motion parameters. Therefore, it can be concluded that the proposed method can be utilized to imaging of targets with different motion parameters compared with PGA, WVD, and IHAF_ICPF.

D. ISAR Imaging With EM Data

In order to further verify the performance of the proposed method in a more realistic environment, in this section, the radar cross-section (RCS) data are produced using an EM scattering
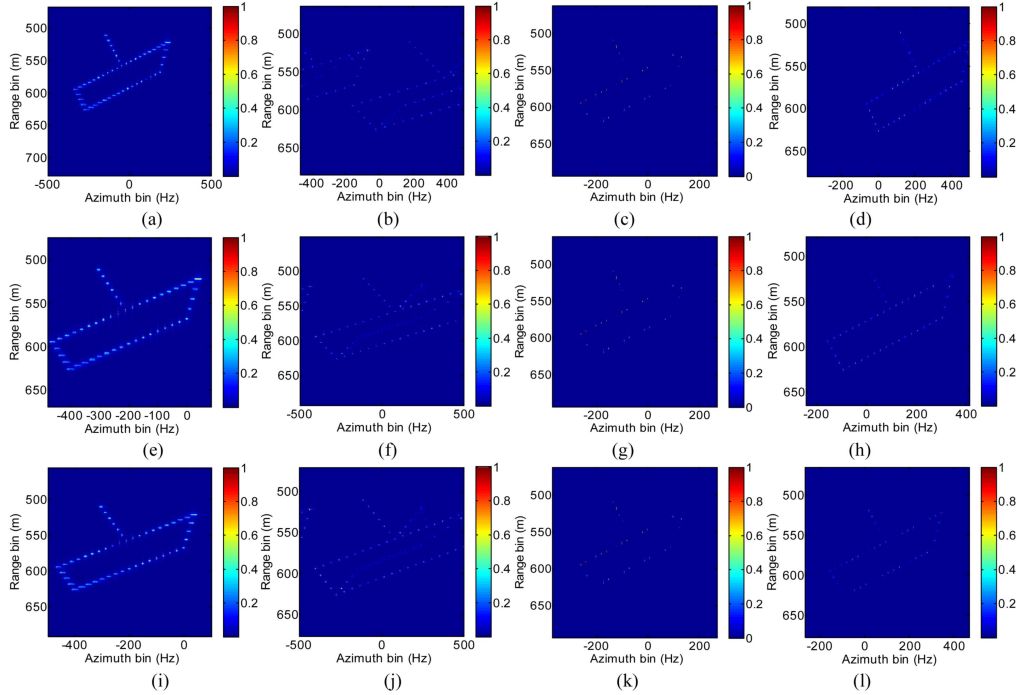
Fig. 10. Imaging results under different motion parameters with different imaging method. (a)–(d) Imaging results of PGA, WVD, IHAF_ICPF and the proposed method under case one, respectively. (e)–(h) Imaging results of PGA, WVD, IHAF_ICPF and the proposed method under case two, respectively. (i)–(l) Imaging results of PGA, WVD, IHAF_ICPF and the proposed method under case three, respectively.

TABLE V
TARGET MOTION PARAMETERS

Velocity / Case	Target RM parameters (rad/s)						TM parameters	
	ω_y	ω_p	ω_r	ω_r'	ω_y'	ω_p'	v	α
Case One	-0.2	0.12	-0.06	0.1	5.5e-2	-2.5e-2	10	1
Case Two	0.1	-0.1	-0.3	6.3e-3	5.5e-2	-2.5e-2	10	1
Case Three	-0.121	0.1	-1e-2	3.5e-2	5.5e-2	-2.5e-2	15	2

prediction technique, which is an effective and economical way to obtain the radar echoes for noncooperative targets with complex motions. The well-known physical optical technique [34], which is one of the widely adopted techniques for high-frequency EM computation, is utilized to generate the RCS data. The original target model is provided in Fig. 11(a). The imaging results obtained by PGA, WVD, IHAF_ICPF, and the proposed method are provided in Fig. 11(b)–(e), respectively. What is noteworthy is that, from Fig. 11, the method of PGA, WVD, and the proposed method can reconstruct the contours of the targets. In addition, the contours of the imaging results using the WVD method are broadened, shown in Fig. 11(c). Furthermore, the contours of the imaging results with the IHAF_ICPF method are obscure in contrast to that of other approaches. Moreover, to further evaluate the quality of imaging results, the image entropy, contrast, and the imaging time of each method are summarized in Table VI, where the image entropy of the imaging results by using the proposed method is less than that of the PGA and WVD method, and the contrast of the imaging results of the proposed method is larger than that of the PGA and WVD

TABLE VI
COMPARISON OF IMAGE ENTROPY, CONTRAST, AND IMAGING TIME

Method / Items	PGA	WVD	IHAF_ICPF	Proposed Method
Entropy	7.6257	6.553	--	4.22
Contrast	174.91	168	--	433.43
Time/s	0.66	52.39	1240545.55	3.05

method. The running times of different method are consistent with the simulation results in Table III. Therefore, considering the tradeoff between the imaging quality and imaging efficiency, the proposed method is a promising candidate.

VI. DISCUSSION

ISAR imaging for targets plays an important role in target detection and recognition thanks to the all-weather, and all-day. However, for noncooperative targets with complex TM and 3-D RM, the echoes are companied by SV phase error and high-order
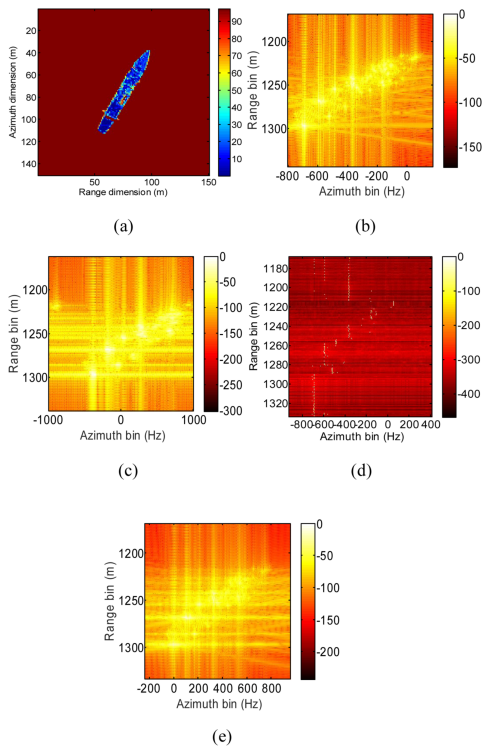
Fig. 11.   Imaging results with different methods. (a) Original model. (b) PGA method. (c) WVD method. (d) IHAF_ICPF method. (e) Proposed method.

phase error, resulting in poor imaging performance due to the cascaded compensating mode for TM and RM, especially under low SNR condition. To obtain high-quality ISAR images for noncooperative with complex TM and 3-D RM, in this work, the time-varying instantaneous slant range is introduced where the LOS is modeled as a function about slow time. In addition, to eliminate the phase error caused by the cascade compensation operation, the TM phase error is compensated for by utilizing the signal that contains prominent scatterers, which can avoid the residual TM phase error. Meanwhile, to obtain the signal with prominent scatterers, the similarity between the profiles of echoes is explored to generate an adaptive denoising filter for mitigating the effects of noise. The signal coherence is fully utilized in the azimuth dimension to compensate for the SV phase errors caused by the RM. The experimental results using simulations and EM data demonstrate that the proposed method has a tradeoff between imaging efficiency and imaging quality.

Up to now, the ISAR imaging principle of most existing approaches is that the 3-D structure of the targets is projected onto a 2-D plane, resulting in an unintuitive target details. Therefore, as a continuation of the work, from the view of target recognition, we can explore the approaches for reconstructing 3-D structure of ship targets.

VII. Conclusion

Due to the complex motions of noncooperative, e.g., TM and 3-D RD, existing algorithms cannot obtain satisfactory results. As a result, in this work, an efficient ISAR imaging method

for noncooperative targets with complex motion is proposed. First, the geometry and signal model for noncooperative targets TM and 3-D RM are established, where the high-order 2-D SV phase error are deduced by utilizing a nonstationary IPP model. Second, to mitigate the influence of noise, an adaptive denoising filter is generated by exploring the similarity between the profiles of echoes. In addition, inspired by the characteristic that all scatterers share the same TM, the compensating factors are extracted from the prominent scatterers, which can absolutely avoid the accumulation of residual TM errors. Meanwhile, the signal coherence is fully utilized to compensate for the SV phase errors caused by the RM. The main contributions are as follows.

1) To reasonably describe the mobility of the noncooperative targets with TM and 3-D RM, the geometry and signal model with nonstationary IPP are established, where the high-order phase model is deduced to describe the 2-D SV phase errors.
2) By exploring the similarity between the profiles of echoes, an adaptive denoising filter is generated to mitigate the influence of noise for the purpose of extracting prominent scatterers.
3) Compared with the existing TM phase error compensation methods based on parameter estimation, the proposed method fully utilizes the signal itself as a compensating factor, which can absolutely avoid the accumulation of residual errors. Additionally, the signal coherence is fully utilized to compensate for the TM error. The experimental results using the simulated and EM data demonstrate the effectiveness and robustness of the proposed method.

References

[1] D. R. Wehner, *High Resolution Radar*. Norwood, MA, USA: Artech House, 1995.
[2] C. Ozdemir, *Inverse Synthetic Aperture Radar Imaging With MATLAB Algorithms*. Hoboken, NJ, USA: Wiley, 2012.
[3] X. H. Tan et al., "An efficient range-doppler domain ISAR imaging approach for rapidly spinning targets," *IEEE Trans. Geosci. Remote Sens.*, vol. 58, no. 4, pp. 2670–2681, Apr. 2020.
[4] F. Berizzi and M. Diani, "ISAR imaging of rolling, pitching and yawing targets," in *Proc. Int. Radar Conf. Int. Commission Illumination*, 1996, pp. 346–349.
[5] Z. Liu, Y. Jiang, Y. Wang, and Y. Du, "Radar imaging of nonstationary rotating ship target with GEO-shipborne bistatic configuration," *IEEE Sensors J.*, vol. 19, no. 13, pp. 5213–5218, Jul. 2019.
[6] P. O'Shea, "A fast algorithm for estimating the parameters of a quadratic FM signal," *IEEE Trans. Signal Process.*, vol. 52, no. 2, pp. 385–393, Feb. 2004.
[7] Y. Wang and Y. Jiang, "Inverse synthetic aperture radar imaging of maneuvering target based on the product generalized cubic phase function," *IEEE Geosci. Remote Sens. Lett.*, vol. 8, no. 5, pp. 958–962, Sep. 2011.
[8] D. Li, M. Zhan, J. Su, H. Liu, and G. Liao, "Performances analysis of coherently integrated cubic phase function for LFM signal and its application to ground moving target imaging," *IEEE Trans. Geosci. Remote Sens.*, vol. 55, no. 11, pp. 6402–6419, Nov. 2017.
[9] Y. Wang, J. Kang, and Y. Jiang, "ISAR imaging of maneuvering target based on the local polynomial Wigner distribution and integrated high-order ambiguity function for cubic phase signal model," *IEEE J. Sel. Topics Appl. Earth Observ. Remote Sens.*, vol. 7, no. 7, pp. 2971–2991, Jul. 2014.
[10] V. C. Chen and W. J. Miceli, "Time-varying spectral analysis for radar imaging of maneuvering targets," *IEE Proc.-Radar Sonar Navigation*, vol. 145, pp. 262–268, Oct. 1998.
[11] T. A. C. M. Classen and W. F. G. Mecklenbrauker, "The Wigner Distribution-a tool for time-frequency signal analysis-Part II: Discrete time signals," *Philips J. Res.*, vol. 35, no. 3, pp. 217–250, 1980.

[12] G. Hajduch, J. M. L. Caillec, and R. Garello, "Airborne high-resolution ISAR imaging of ship targets at sea," *IEEE Trans. Aerosp. Electron. Syst.*, vol. 40, no. 1, pp. 378–384, Jan. 2004.

[13] D. Pastina and C. Spina, "Slope-based frame selection and scaling technique for ship ISAR imaging," *Inst. Eng. Technol. Signal Process.*, vol. 2, no. 3, pp. 265–276, Sep. 2008.

[14] H. Sun, M. Xing, and L. Zhou, "Divison of imaging intervals and selection of optimum imgaging time for ship ISAR imaging based on measured data," in *Proc. Int. Commission Illumination Int. Conf. Radar*, 2006, pp. 1–4.

[15] T. Itoh, H. Sueda, and Y. Watanabe, "Motion compensation for ISAR via centroid tracking," *IEEE Trans. Aerosp. Electron. Syst.*, vol. 32, no. 3, pp. 1191–1197, Jul. 1996.

[16] D. E. Wahl, P. H. Eichel, D. C. Ghiglia, and C. V. Jakowatz, "Phase gradient autofocus-a robust tool for high resolution SAR phase correction," *IEEE Trans. Aerosp. Electron. Syst.*, vol. 30, no. 3, pp. 827–835, Jul. 1994.

[17] H. Wu, D. Grenier, G. Y. Delisle, and D.-G. Fang, "Translational motion compensation in ISAR image processing," *IEEE Trans. Image Process.*, vol. 4, no. 11, pp. 1561–1571, Nov. 1995.

[18] T. Itoh, H. Sueda, and Y. Watanabe, "Motion compensation for ISAR via centroid tracking," *IEEE Trans. Aerosp. Electron. Syst.*, vol. 32, no. 3, pp. 1191–1197, Jul. 1996.

[19] R. Wang, T. Zeng, C. Hu, J. Yang, and T. Long, "Accurate range profile alignment method based on minimum entropy for inverse synthetic aperture radar image formation," *Inst. Eng. Technol. Radar, Sonar Navigation*, vol. 10, no. 4, pp. 663–671, Apr. 2016.

[20] P. Cao, M. Xing, G. Sun, Y. Li, and Z. Bao, "Minimum entropy via subspace for ISAR autofocus," *IEEE Geosci. Remote Sens. Lett.*, vol. 7, no. 1, pp. 205–209, Jan. 2010.

[21] L. Zhao, L. Wang, G. Bi, and L. Yang, "An autofocus technique for high-resolution inverse synthetic aperture radar imagery," *IEEE Trans. Geosci. Remote Sens.*, vol. 52, no. 10, pp. 6392–6403, Oct. 2014.

[22] Y. Xiang, Z. Dai-Yin, Z. Jing-Dong, and J. Rui, "Motion compensation algorithm based on the designing structured Gram matrices method," *Inst. Eng. Technol. Radar, Sonar Navigation*, vol. 8, no. 3, pp. 209–219, Mar. 2014.

[23] H. Fan, L. Ren, E. Mao, and Q. Liu, "A high-precision method of phase-derived velocity measurement and its application in motion compensation of ISAR imaging," *IEEE Trans. Geosci. Remote Sens.*, vol. 56, no. 1, pp. 60–77, Jan. 2018.

[24] K. Patel, U. Neelakantan, S. Gangele, J. G. Vacchani, and N. M. Desai, "Linear frequency modulation waveform synthesis," in *Proc. IEEE Students' Conf. Elect., Electron. Comput. Sci.*, 2012, pp. 1–4.

[25] J. Li, H. Ling, and V. Chen, "An algorithm to detect the presence of 3D target motion from ISAR data," *Multidimensional Syst., Signal Process.*, vol. 14, no. 1–3, pp. 223–240, Jan. 2003.

[26] J. Wang, L. Zhang, L. Du, D. Yang, and B. Chen, "Noise-robust motion compensation for aerial maneuvering target ISAR imaging by parametric minimum entropy optimization," *IEEE Trans. Geosci. Remote Sens.*, vol. 57, no. 7, pp. 4202–4217, Jul. 2019.

[27] R. P. Paul, *Robot Manipulators: Mathematics, Programming, and Control.* Cambridge, MA, USA: MIT Press, 1986.

[28] L. Xi, L. Guosui, and J. Ni, "Autofocusing of ISAR images based on entropy minimization," *IEEE Trans. Aerosp. Electron. Syst.*, vol. 35, no. 4, pp. 1240–1252, Oct. 1999.

[29] F. Berizzi, M. Martorella, A. Cacciamano, and A. Capria, "A contrast-based algorithm for synthetic range-profile motion compensation," *IEEE Trans. Geosci. Remote Sens.*, vol. 46, no. 10, pp. 3053–3062, Oct. 2008.

[30] B. S. Kang, M. S. Kang, I. O. Choi, C. H. Kim, and K. T. Kim, "Efficient autofocus chain for ISAR imaging of non-uniformly rotating target," *IEEE Sensors J.*, vol. 17, no. 17, pp. 5466–5478, Sep. 2017.

[31] D. Huang, C. Feng, N. Tong, and Y. Guo, "2D spatial-variant phase errors compensation for ISAR imagery based on contrast maximization," *Electron. Lett.*, vol. 52, no. 17, pp. 1480–1482, Jul. 2016.

[32] L. Liu, F. Zhou, M.-L. Tao, B. Zhao, and Z.-J. Zhang, "Cross-range scaling method of inverse synthetic aperture radar image based on discrete polynomial-phase transform," *Inst. Eng. Technol. Radar, Sonar Navigation*, vol. 9, no. 3, pp. 333–341, Mar. 2015.

[33] J. Sheng, M. Xing, L. Zhang, M. Q. Mehmood, and L. Yang, "ISAR cross-range scaling by using sharpness maximization," *IEEE Geosci. Remote Sens. Lett.*, vol. 12, no. 1, pp. 165–169, Jan. 2015.

[34] R. G. Kouyoumjian, "Asymptotic high-frequency methods," *Proc. IEEE*, vol. 53, no. 8, pp. 864–876, Aug. 1965.

Zhijun Yang (Member, IEEE) was born in Chongqing, China, in 1991. He received the Ph.D. degree in electrical engineering from Chongqing University, Chongqing, China, in 2021.

He is currently a Postdoctoral Researcher with the Beijing Institute of Technology Chongqing Innovation Center, Chongqing, China. His research interests include inverse synthetic aperture radar imaging, and differential interferometric SAR (DInSAR) technology.

Xiaoheng Tan received the B.E. and Ph.D. degrees in electrical engineering from Chongqing University, Chongqing, China, in 1998 and 2003, respectively.

He was a Visiting Scholar with the University of Queensland, Brisbane, Qld., Australia, from 2008 to 2009. He is currently a Professor with the School of Microelectronics and Communication Engineering, Chongqing University. His current research interests include modern communications technologies and systems, radar signal processing, and machine learning.

Weiming Tian (Member, IEEE) was born in 1983. He received the B.S. and Ph.D. degrees in electrical engineering from the Beijing Institute of Technology, Beijing, China, in 2005 and 2010, respectively.

He is currently working with the School of Information and Electronics, Beijing Institute of Technology. His research interests include synthetic aperture radar (SAR) system design and signal processing, bistatic SAR synchronization, and differential interferometric SAR (DInSAR) technology.

Xichao Dong (Member, IEEE) received the B.S. degree in electrical engineering and the Ph.D. degree in target detection and recognition from the Beijing Institute of Technology (BIT), Beijing, China, in 2008 and 2014, respectively.

From 2011 to 2013, he was a Research Assistant with the Centre for Terrestrial Carbon Dynamics (CTCD), University of Sheffield, Sheffield, U.K. From 2014 to 2017, he held a Postdoctoral position with the School of Information and Electronics, BIT. Since 2017, he has been an Assistant Professor with the School of Information and Electronics, BIT. Since December 2019, he has been with the BIT Chongqing Innovation Center, Chongqing, China. His research interests include geosynchronous synthetic aperture radar and weather radar.

Dr. Dong was the recipient of the IEEE CIE International Radar Conference Excellent Paper Award in 2011 and the Chinese Institute of Electronics Youth Conference Poster Award in 2014.

Chang Cui (Member, IEEE) was born in Hunan, China, in 1994. She received the B.S. and Ph.D. degrees in electrical engineering from the School of Information and Electronics, Beijing Institute of Technology, in 2016 and 2022, respectively.

She is currently a Postdoctoral Researcher with the Beijing Institute of Technology Chongqing Innovation Center, Chongqing, China. Her research interests include geosynchronous synthetic aperture radar signal processing and moving target indication.